



1 **Land Surface Model Representation of the Mutual Information**
2 **Context between Multi-Layer Soil Moisture and**
3 **Evapotranspiration**

4 Jianxiu Qiu^{1,2}, Wade T. Crow³, Jianzhi Dong³, Grey S. Nearing⁴

5 ¹Guangdong Provincial Key Laboratory of Urbanization and Geo-simulation, School of Geography and Planning, Sun
6 Yat-sen University, Guangzhou, 510275, China

7 ²Southern Laboratory of Ocean Science and Engineering (Guangdong, Zhuhai), Zhuhai, 519000, China

8 ³USDA ARS Hydrology and Remote Sensing Laboratory, Beltsville, MD 20705, USA

9 ⁴Department of Geological Sciences, University of Alabama, AL 35487, USA

10 *Correspondence to:* Jianxiu Qiu (qiujianxiu@mail.sysu.edu.cn)



11 **Abstract.** Soil moisture (θ) impacts the climate system by regulating incoming energy into outgoing
12 evapotranspiration (ET) and sensible heat flux components. Therefore, investigating the coupling strength between θ
13 and ET is important for the study of land surface/atmosphere interactions. Here, we use in-situ AmeriFlux observations
14 to evaluate θ /ET coupling strength estimates acquired from multiple land surface models (LSMs). For maximum
15 robustness, coupling strength is represented using the sampled normalized mutual information (NMI) between θ
16 estimates acquired at various vertical depths and surface flux represented by fraction of potential evapotranspiration
17 (fPET, the ratio of ET to potential ET). Results indicate that LSMs are generally in agreement with AmeriFlux
18 measurements in that surface soil moisture (θ_s) contains slightly more NMI with fPET than vertically integrated soil
19 moisture (θ_v). Overall, LSMs adequately capture variations in NMI between fPET and θ estimates acquired at various
20 vertical depths. However, one model – the Global Land Evaporation Amsterdam Model (GLEAM) – significantly
21 overestimates the NMI between θ and ET and the relative contribution of θ_s to total ET. This bias appears attributable
22 to differences in GLEAM’s ET estimation scheme relative to the other two LSMs considered here (i.e., the Noah with
23 Multi-parameterization option and the Catchment Land Surface Model). These results provide insight into improved
24 LSM model structure and parameter optimization for land surface-atmosphere coupling analyses.

25 **Keywords.** Land surface/atmosphere interaction, soil moisture, surface evapotranspiration

26 **1 Introduction**

27 Soil moisture (θ) modulates water and energy feedbacks between the land surface and the lower atmosphere by
28 partitioning incoming energy into evapotranspiration (ET) and sensible heat (H) surface flux components (Seneviratne
29 et al., 2010, 2013). In water-limited regimes, θ exhibits a dominant control on ET and, therefore, commonly exerts
30 significant terrestrial control on the earth’s water, energy and biochemical cycles. Accurately representing θ /ET
31 coupling in land surface models (LSMs) is therefore expected to improve our ability to project the future frequency
32 of extreme climates (Seneviratne et al., 2013).

33 A key question is how the constraint of θ on ET and H varies as θ is vertically integrated over deeper vertical soil
34 depths. Given the tendency for the time scales of θ dynamics to vary strongly with depth, the degree to which the ET
35 is coupled with vertical variations in θ determines the temporal scale at which θ variations are propagated into the
36 atmosphere. Therefore, in order to represent θ /ET coupling, and thus land/atmosphere interactions in general, LSMs
37 must accurately capture the relationship between vertically varying θ values and ET. Unfortunately, their abilities to
38 do so remains an open question.

39 Recently, land surface/atmosphere coupling strength has been investigated by sampling mutual information proxies
40 (e.g., correlation coefficient or other coupling indices) between time series of θ and ET (or air temperature proxies for
41 ET). Results suggest that, even when confined to very limited vertical support (e.g., within the top 5 cm of the soil
42 column), surface θ estimates retain significant information for examining θ controls on local climate (Ford and Quiring,
43 2014b; Qiu et al., 2014; Dong and Crow, 2018; Dong and Crow, 2019). These findings are in contrast with the common



44 perceptions that ET is dominated by θ values at deeper soil layers (Hirschi et al., 2014). Hence, it is necessary to
45 examine whether LSMs can realistically reflect observed variations of θ /ET coupling strength in the vertical soil
46 profiles.

47 Previous studies examining the θ /ET relationship have generally been based on Pearson product-moment correlation
48 (Basara and Crawford, 2002; Ford et al., 2014a), which captures only the strength of a linear relationship between two
49 variables. However, the coupling between θ and ET is generally nonlinear. Therefore, non-parametric mutual
50 information measures are generally more appropriate. Nearing et al. (2018) used information theory metrics (transfer
51 entropy, in particular) to measure the strengths of directed couplings between different surface variables, including
52 soil moisture, and surface energy fluxes at short timescales in several LSMs. They found that the LSMs were generally
53 biased as compared with strengths of couplings in observation data, and that these biases differed across different
54 study sites. However, they did not look at the effect of vertical moisture profiles or of subsurface soil moisture on
55 partitioning surface energy fluxes.

56 Here we apply the information theory-based methodology of Qiu et al. (2016) to examine the relationship between
57 the vertical support of θ estimates and their mutual information (MI) with respect to ET. Our approach is based on
58 analyzing the MI content between ET and θ time series - acquired from both LSMs and AmeriFlux in-situ observations.
59 MI values are then normalized by corresponding ET entropy to remove the effect of inter-site variation and generate
60 estimates of Normalized Mutual Information (NMI) between θ and ET. Examined θ time series have two different
61 vertical supports: surface soil moisture (θ_s) and vertically integrated soil moisture (θ_v). AmeriFlux NMI results are
62 compared with analogous NMI results obtained from LSM-based θ and ET time series.

63 Further details on our methodology are presented in Sect. 2. Results are presented in Sect. 3 and discussed/summarized
64 in Sect. 4.

65 **2 Data and Methods**

66 The AmeriFlux network provides temporally continuous measurements of θ , surface energy fluxes and related
67 environmental variables for sites located in a variety of North American ecosystem types, e.g., forests, grasslands,
68 croplands, shrublands and savannas (Boden, et al., 2013). To minimize sampling errors, AmeriFlux sites lacking a
69 complete 3-year summer months (June, July and August) daily time series between the years of 2003 and 2015 (i.e.,
70 $3 \times 92 = 276$ daily observations in total) of θ_s , θ_v and latent heat flux (LE) were excluded here - resulting in the 34
71 eligible AmeriFlux sites listed in Table 1. These sites cover a variety of climate zones within the contiguous United
72 States (CONUS). Table 1 gives background information on these 34 sites including local land cover information.
73 Hydro-climatic conditions in each site were characterized using the aridity index (AI) - calculated using CRU (Climate
74 Research Unit, v4.02) monthly precipitation and potential evaporation (PET) datasets.

75 As described above, θ /ET coupling assessments made using AmeriFlux observations were compared with comparable
76 assessments based on output from state-of-the-art LSMs including Noah with Multi-parameterization option



77 (NOAHMP), Catchment Land Surface Model (CLSM), and Global Land Evaporation Amsterdam Model (GLEAM).
 78 See below for more model details. To avoid any spurious correlations between θ and ET due to seasonality, all NMI
 79 analyses were performed on θ and ET time series anomalies acquired during the period 2003–2015. The θ and ET
 80 anomalies were calculated by removing the seasonal cycle – defined as 31-day window averages centered on each
 81 day-of-year sampled across all years of the 2003–2015 historical data record – from the raw θ and ET time series data.
 82 The analysis was limited to the CONUS during summer months (June, July and August) when θ /ET coupling was
 83 expected to be maximized.

84

Table 1 Attributes of selected AmeriFlux sites

AmeriFlux sites	Land cover	Elevation [m]	Top- layer depth [cm]	Bottom- layer depth [cm]
ARM SGP Main	Cropland	314	10 ^a	20 ^b
ARM USDA UNL OSU Woodward Switchgrass 1	Grassland	611	10	30
Audubon Research Ranch	Grassland	1469	10	20
Bondville	Cropland	219	10 ^c	20
Brookings	Grassland	510	10	20
Chimney Park	Evergreen needleleaf forest	2750	0-15	15-45
Duke Forest Hardwoods	Deciduous broadleaf forest	168	10	25
Duke Forest Open Field	Grassland	168	10	25
Fermi Agricultural	Cropland	225	2.5	10
Fermi Prairie	Grassland	226	2.5	10
Flagstaff Managed Forest	Evergreen needleleaf forest	2160	2	10
Flagstaff Unmanaged Forest	Woody savannas	2180	2	10
Flagstaff Wildfire	Grassland	2270	2	10
Fort Peck	Grassland	634	5 ^d	20
Freeman Ranch Woodland	Woody savannas	232	10	20
Glacier Lakes Ecosystem Experiments Site	Evergreen needleleaf forest	3190	5	10
Howland Forest Main	Mixed forest	60	NA	NA
Lucky Hills Shrubland	Open shrubland	1372	5	15
Marys River Fir Site	Evergreen needleleaf forest	263	10	20
Metolius Intermediate Pine	Evergreen needleleaf forest	1253	0-30	NA
Missouri Ozark	Deciduous broadleaf forest	219	10	100
Nebraska SandHills Dry Valley	Grassland	1081	10	25
Quebec Boreal Cutover Site	Evergreen needleleaf forest	400	5	20
Quebec Mature Boreal Forest Site	Evergreen needleleaf forest	400	5	10
Santa Rita Creosote	Open shrubland	991	2.5	12.5
Santa Rita Mesquite	Woody savannas	1116	2.5-5	5-10
Sherman Island	Grassland	-5	10	20
Sylvania Wilderness	Mixed forest	540	5	10
Tonzi Ranch	Woody savannas	169	0	20



University of Michigan Biological Station	Deciduous broadleaf forest	234	0-30	NA
Vaira Ranch	Grassland	129	0	10
Walker Branch	Deciduous broadleaf forest	343	5	10
Willow Creek	Deciduous broadleaf forest	515	5	10
Wind River Field Station	Evergreen needleleaf forest	371	30 ^e	50 ^f

85

86 ^a Was 5 cm prior to 4/13/2005

87 ^b Was 25 cm prior to 4/13/2005

88 ^c Was 5 cm prior to 1/1/2006

89 ^d Was 10 cm (2003-2008)

90 ^e Was 0-30 cm prior to 2007

91 ^f Was NaN prior to 2007

92 2.1 Ground-based AmeriFlux measurements

93 The Level 2 (L2) AmeriFlux LE and sensible heat (H) flux observations are based on high-frequency (typically > 10
94 Hz) eddy covariance measurements processed into half-hourly averages by individual AmeriFlux investigators. LE
95 and θ observations at a half-hour time step and without gap-filling procedures were collected from the AmeriFlux Site
96 and Data Exploration System (see <http://ameriflux.ornl.gov/>). The LE and θ observations were further aggregated into
97 daily (0 to 24 UTC) values, and daily LE was converted into daily ET using the latent heat of vaporization. Daily ET
98 values based on less than 30% half-hourly coverage (i.e., < 15 half-hourly observations per day) were considered not
99 representative at a daily time scale and therefore excluded.

100 Soil moisture measurements are generally available at two discrete depths that vary between the AmeriFlux sites
101 (Table 1). Here, the top (i.e., closest to the surface) soil moisture observation was always used to represent surface
102 soil moisture (θ_s). Since the depth of this top layer measurement varies between 0 and 15 cm (see Table 1), we consider
103 the surface-layer measurement θ_s to be roughly representative of 0–10 cm (vertically integrated) θ .

104 Given variations in the depth of the lower AmeriFlux θ observations (see Table 1), we applied a variety of approaches
105 for estimating vertically integrated soil moisture (θ_v). Our first approach, hereinafter referred to as Case I, was based
106 on the application of an exponential filter (Wagner et al., 1999; Albergel et al., 2008) to extrapolate θ_s to a consistent
107 40 cm bottom layer depth. Therefore, only θ_s was used to derive θ_v and the bottom-layer AmeriFlux θ measurement
108 was neglected in this case. The application of the exponential filter requires a single time-scale parameter T . Since θ
109 measurements from United States Department of Agriculture's Soil Climate Analysis Network (SCAN) are taken at
110 fixed soil depth, we utilized this dataset to determine the most appropriate parameter T at AmeriFlux sites. Following
111 Qiu et al. (2014), first, we estimated the optimal parameter T (T_{opt}) for the extrapolation of θ measurements from 10
112 cm to 40 cm depth and established a global relationship between T_{opt} and site-based NDVI (MOD13Q1 v006, 250m,
113 16-day) ($T_{opt} = 2.098 \times \exp(-1.895 \times (\text{NDVI} + 0.6271)) + 2.766$). Then, this global relationship (Goodness of Fit R^2 :
114 0.85) was applied to AmeriFlux sites to extrapolate 0–10 cm θ_s times series into 0–40 cm θ_v .



115 Previous research has suggested that such a filtering approach does not significantly squander ET information present
116 in actual measurements of θ_v (Qiu et al., 2014; Qiu et al., 2016). Nevertheless, since the quality of θ_v estimates is
117 important in our analysis, we also calculated two addition cases where 0–40 cm θ_v was estimated using: 1) the bottom-
118 layer soil moisture measurement acquired at each AmeriFlux site (hereinafter, Case II) and 2) linear interpolation of
119 θ_s and the bottom-layer AmeriFlux soil moisture measurement (hereinafter, Case III). The sensitivity of key results to
120 these various cases is discussed below.

121 2.2 LSM-based simulations

122 LSM output was acquired from NOAHMP (Niu et al., 2011) and CLSM (Koster et al., 2000) simulations embedded
123 within the NASA Land Information System (LIS, Kumar et al., 2006) and a satellite-observation-based model
124 GLEAM (Miralles et al., 2011). Both NOAHMP and CLSM were set-up to simulate 0.125 ° θ profiles at a 15-minute
125 time step using North America Land Data Assimilation System, Phase 2 (NLDAS-2) forcing data. A 10-year model
126 spin-up period (1992 to 2002) was applied for NOAHMP and CLSM.

127 NOAHMP numerically solves the one-dimensional Richards equation within four soil layers of thicknesses of 10, 30,
128 60, and 100 cm. Major parameterization options relevant to θ simulation include: 1) options for canopy stomatal
129 resistance; 2) options for θ factor for stomatal resistance (the β factor). Here we employed the Ball-Berry-type stomatal
130 resistance scheme and Noah-type soil moisture factor controlling the β factor. The specific expressions are as follows:

$$131 \quad \beta = \sum_{i=1}^{N_{\text{root}}} \frac{\Delta z_i}{z_{\text{root}}} \min \left(1.0, \frac{\theta_i - \theta_{\text{wilt}}}{\theta_{\text{ref}} - \theta_{\text{wilt}}} \right) \quad (1)$$

132 where θ_{wilt} and θ_{ref} are respectively soil moisture at wilting point ($\text{m}^3 \text{m}^{-3}$) and reference soil moisture ($\text{m}^3 \text{m}^{-3}$), which
133 is close to field capacity. θ_i and Δz_i are soil moisture ($\text{m}^3 \text{m}^{-3}$) and soil depth (cm) at i th layer, N_{root} and z_{root} are total
134 number of soil layers with roots and total depth (cm) of root zone, respectively.

135 Following the Ball-Berry stomatal resistance scheme, the θ -controlled β factor and other multiplicative factors
136 including temperature, foliage nitrogen simultaneously determine the maximum carboxylation rate V_{max} as follows:

$$137 \quad V_{\text{max}} = V_{\text{max}25} \alpha_{\text{vmax}}^{\frac{T_v - 25}{10}} f(N) f(T_v) \beta \quad (2)$$

138 where $V_{\text{max}25}$ is maximum carboxylation rate at 25 °C ($\mu\text{mol CO}_2 \text{m}^{-2} \text{s}^{-1}$); α_{vmax} is a parameter sensitive to vegetation
139 canopy surface temperature T_v ; $f(N)$ is a factor representing foliage nitrogen and $f(T_v)$ is a function that mimics thermal
140 breakdown of metabolic processes. Based on V_{max} , carboxylase-limited (Rubisco limited) and export-limited (for C3
141 plants) photosynthesis rates per unit LAI (A_C and A_S respectively) are calculated, and the minimum of A_C , A_S and light-
142 limited photosynthesis rates determine stomatal conductance r_s , and, consequently, the ET over vegetated areas. For
143 the complete NOAHMP configuration, please see Table S1 in the supplementary material.



144 CLSM simulates the 0–2 and 0–100 cm soil moisture and evaporative stress as a function of simulated θ and
145 environmental variables. ET is then estimated based on the estimated evaporative stress and land-atmosphere humidity
146 gradients. Energy and water flux estimates are iterated with soil state estimates (e.g., θ and soil temperature) to ensure
147 closure of surface energy and water balances. For the detailed explanation of CLSM, please refer to Koster et al.
148 (2000).

149 GLEAM is a set of algorithms dedicated to the estimation of terrestrial ET and root-zone θ from satellite data. In this
150 study, the latest version of this model (v3.2a) is employed. In GLEAM, the configuration of soil layers varies as a
151 function of the land-cover type. Soil stratification is based on three soil layers for tall vegetation (0–10, 10–100, and
152 100–250 cm), two layers for low vegetation (0–10, 10–100 cm) and only one layer for bare soil (0–10 cm) (Martens
153 et al., 2017).

154 The cover-dependent PET (mm day^{-1}) of GLEAM is calculated using the Priestley and Taylor (1972) equation based
155 on observed air temperature and net radiation. Following this, estimates of PET were converted into actual
156 transpiration or bare soil evaporation (depending on the land-cover type, ET (mm day^{-1})), using a cover-dependent,
157 multiplicative stress factor S (–), which is calculated as a function of microwave vegetation optical depth (VOD) and
158 root-zone θ (Miralles et al., 2011). The related expressions are as follows:

$$159 \quad \text{ET} = \text{PET} \times S + E_i \quad (3)$$

$$160 \quad S = \sqrt{\frac{\text{VOD}}{\text{VOD}_{\max}}} \left(1 - \left(\frac{\theta_c - \theta_\omega}{\theta_c - \theta_{\text{wilt}}} \right)^2 \right) \quad (4)$$

161 where E_i is rainfall interception (mm); S essentially represents the fPET (see Sect. 2.3) estimated by GLEAM; θ_c (m^3
162 m^{-3}) is the critical soil moisture and θ_ω ($\text{m}^3 \text{m}^{-3}$) is the soil moisture content of the wettest layer, assuming that plants
163 withdraw water from the layer that is most accessible. Based on (4), GLEAM S (or fPET) tend to become more
164 sensitive to θ in areas of low VOD seasonality (i.e., low differences between VOD and VOD_{\max}). As for bare soil
165 conditions, S is linearly related to surface soil moisture (θ_1):

$$166 \quad S = 1 - \frac{\theta_c - \theta_1}{\theta_c - \theta_{\text{wilt}}} \quad (5)$$

167 To resolve variations in the vertical discretization of θ applied by each model, we linearly interpolated NOAAHMP,
168 CLSM and GLEAM outputs into daily 0–10 and 0–40 cm soil moisture values using depth-weighted averaging.

169 **2.3 Variable indicating soil moisture and surface flux coupling**

170 Soil moisture – ET coupling can be diagnosed using a variety of different variables derived from ET, e.g. the fraction
171 of PET (fPET, the ratio of ET and PET) or the evaporative fraction (EF, the ratio of LE and the sum of LE and sensible
172 heat). Since ET is strongly tied to net radiation (Rn) (Koster et al., 2009), both fPET and EF are advantageous in that



173 they normalize ET and removing the impact of non-soil moisture influences on ET (e.g., net radiation, wind speed and
174 soil heat flux (G)). However, since sensible heat flux is not provided in the GLEAM dataset, we are restricted here to
175 using fPET.

176 It should be noted that the applied meteorological forcing data for NOAHMP and CLSM were somewhat different
177 from those used for GLEAM. Therefore, to minimize the impact of this difference, NOAHMP and CLSM fPET were
178 computed from North American Regional Reanalysis (NARR) using the modified Penman scheme of Mahrt and Ek
179 (1984) while GLEAM fPET was calculated using its own internal PET estimates. To examine the impact of PET
180 source, AmeriFlux fPET calculations were calculated using both GLEAM- and NARR-based PET values.

181 **2.4 Information measures**

182 Mutual information (MI) (Cover and Thomas, 1991) is a nonparametric measure of correlation between two random
183 variables. MI and the related Shannon-type entropy (Shannon, 1948) are calculated as follows. Entropy about a random
184 variable ζ is a measure of uncertainty according to its distribution p_ζ and is estimated as the expected amount of
185 information from p_ζ sample:

$$186 \quad H(p_\zeta) = E_\zeta [-\ln(p_\zeta(\zeta))]. \quad (6)$$

187 Likewise, MI between ζ and another variable ψ can be thought of as the expected amount of information about variable
188 ζ contained in a realization of ψ and is measured by the expected Kullback-Leibler (KL) divergence (Kullback and
189 Leibler, 1951) between the conditional and marginal distributions over ζ :

$$190 \quad \text{MI}(\zeta; \psi) = E_\psi [D(p_{\zeta|\psi} \parallel p_\zeta)]. \quad (7)$$

191 In this context, the generic random variables ζ and ψ represent fPET and θ (soil moisture) respectively. The observation
192 space of the target random variable fPET was discretized using a fixed bin width. As bin width decreases, entropy
193 increases but mutual information asymptotes to a constant value. On the other hand, increased bin width requires more
194 sample size, which cannot always be satisfied. The trick is choosing a bin width where the NMI values stabilize with
195 sample size. After careful sensitivity analysis, we choose a fixed bin width of 0.25 [-] for fPET and make sure that
196 each AmeriFlux site have enough samples to accurately estimate the NMI, and change of this constant bin width from
197 0.1–0.5 [-] will not significantly alter our conclusions. Following Nearing et al. (2016), a bin width of 0.01 m³ m⁻³ (1%
198 volumetric water content) for θ was applied. Integrations required for MI calculation in Eq. (7) are then approximated
199 as summations over the empirical probability distribution function bins (Paninski, 2003).

200 By definition, the MI between two variables represents the amount of entropy (uncertainty) in either of the two
201 variables that can be reduced by knowing the other. Therefore, the MI normalized by the entropy of the AmeriFlux-
202 based fPET measurements represents the fraction of uncertainty in fPET that is resolvable given knowledge of the soil
203 moisture state (Nearing et al., 2013). Unlike Pearson's correlation coefficient, MI is insensitive to the impact of



204 nonlinear variable transformations. Therefore, it is well suited to describe the strength of the (potentially non-linear)
205 relationship between θ and fPET.

206 Here, we applied this approach to calculate the MI content between soil moisture representing different vertical depths
207 (as reflected by θ_s and θ_v) and fPET at each AmeriFlux site. All estimated site-specific MI were normalized by the
208 entropy of the corresponding AmeriFlux-based fPET measurements to remove the effect of inter-site entropy
209 variations on the magnitude of NMI differences. The resulting normalized MI calculations between both θ_s and θ_v
210 and fPET are denoted as $\text{NMI}(\theta_s, \text{fPET})$ and $\text{NMI}(\theta_v, \text{fPET})$ respectively.

211 **The underestimation of observed θ /ET coupling via the impact of mutually-independent θ and ET errors in AmeriFlux**
212 **observations (Crow et al. 2015) was minimized by focusing on the ratio between $\text{NMI}(\theta_s, \text{fPET})$ and $\text{NMI}(\theta_v, \text{fPET})$.**
213 **To quantify the standard error of NMI differences between various soil moisture products, we applied a nonparametric,**
214 **500-member bootstrapping approach, and calculated pooled average of sampling errors across all sites assuming**
215 **spatially independent sampling error.**

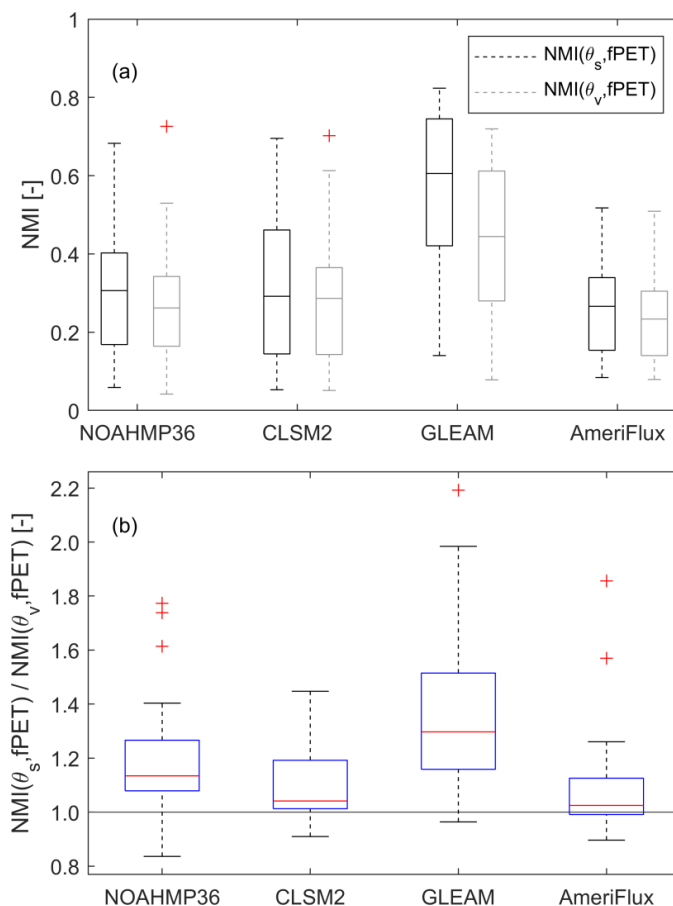
216 Finally, we also examined the impact of potential nonlinearity in the θ /ET relationship by comparing non-parametric
217 NMI results with comparable inferences based on a conventional Pearson's correlation calculation. The correlation-
218 based coupling strength between θ_s and fPET was denoted as $R(\theta_s, \text{fPET})$ and between θ_v and fPET as $R(\theta_v, \text{fPET})$.

219 **3 Results**

220 **3.1 Comparison of $\text{NMI}(\theta_s, \text{fPET})$ and $\text{NMI}(\theta_v, \text{fPET})$**

221 Figure 1 contains boxplots of modelled and observed $\text{NMI}(\theta_s, \text{fPET})$ and $\text{NMI}(\theta_v, \text{fPET})$, i.e., the relative magnitude
222 of fPET information contained in surface soil moisture and **vertically-integrated (0–40 cm) soil moisture**, sampled
223 across all the AmeriFlux locations listed in Table 1. According to the AmeriFlux ground measurements, median values
224 of $\text{NMI}(\theta_s, \text{fPET})$ and $\text{NMI}(\theta_v, \text{fPET})$ (across all sites) are near 0.3 [-]. This suggests that approximately 30% of the
225 uncertainty (i.e., entropy at this particular bin width of 0.25 [-]) in fPET can be eliminated given knowledge of either
226 surface or vertically integrated soil moisture state. This is consistent with earlier results in Qiu et al., (2016) who used
227 similar variables to evaluate θ /EF (evaporative fraction) coupling strength. The sampled medians of $\text{NMI}(\theta_s, \text{fPET})$
228 and $\text{NMI}(\theta_v, \text{fPET})$ estimated by the NOAHMP and CLSM models are similar to these (observation-based) AmeriFlux
229 values. With the single exception that CLSM predicts much larger site-to-site variation in $\text{NMI}(\theta_s, \text{fPET})$.

230 In contrast, $\text{NMI}(\theta_s, \text{fPET})$ and $\text{NMI}(\theta_v, \text{fPET})$ values sampled from GLEAM θ and fPET estimates are biased high
231 (with median $\text{NMI}(\theta_s, \text{fPET})$ and $\text{NMI}(\theta_v, \text{fPET})$ values of about 0.5 and 0.4 [-], respectively) with respect to all other
232 estimates.



233

234 Fig.1 The θ /ET coupling strengths for summertime anomaly time series acquired from various LSMs and AmeriFlux measurements:
 235 (a) $NMI(\theta_s, fPET)$ and $NMI(\theta_v, fPET)$ individually and (b) $NMI(\theta_s, fPET)$ normalized by $NMI(\theta_v, fPET)$.

236 All three LSMs overall exhibit significantly (at $p = 0.05$ [-] confidence, using the 34 AmeriFlux site-located samples
 237 pixels for pair t -test) higher $NMI(\theta_s, fPET)$ compared to $NMI(\theta_v, fPET)$ – implying the surface soil moisture
 238 observation contain more fPET information than vertically-integrated soil moisture. However, the difference between
 239 $NMI(\theta_s, fPET)$ and $NMI(\theta_v, fPET)$ is less discernible in AmeriFlux measurements (Fig. 1(a)).

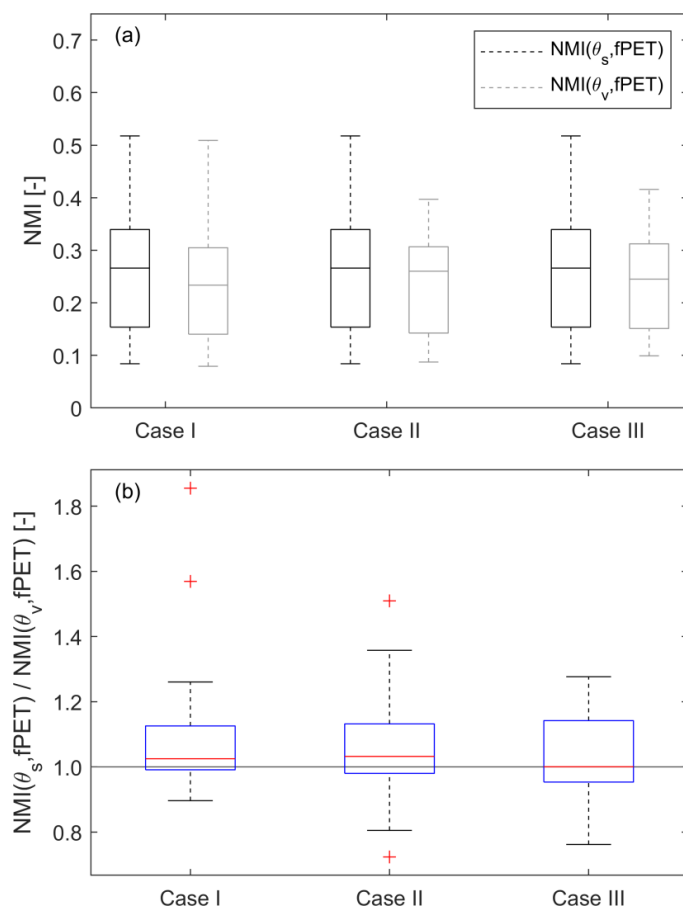
240 Here, AmeriFlux observations are used as a baseline for LSM evaluation. However, it should be stressed that random
 241 observation errors in θ and fPET will introduce a low bias into AmeriFlux-based estimates of both $NMI(\theta_s, fPET)$ and
 242 $NMI(\theta_v, fPET)$ (Crow et al., 2015) and thus their difference as well. To address this concern, Fig. 1(b) plot the ratio
 243 of $NMI(\theta_s, fPET)$ and $NMI(\theta_v, fPET)$, which normalizes and minimizes such observation error impacts. Ratio results
 244 illustrate the general tendency for $NMI(\theta_s, fPET) > NMI(\theta_v, fPET)$ discussed above. They also highlight the tendency
 245 for GLEAM to overvalue θ_s (relative to θ_v) when estimating fPET. A second approach for reducing the random error
 246 of θ and fPET measurement errors is the Triple Collocation (TC)-based correction applied in Crow et al. (2015).



247 However, this approach is currently restricted to linear correlation and cannot be applied to NMI. Future work will
 248 examine extending the information-based TC approach of Nearing et al. (2017), to the examination of NMI.

249 **3.2 Sensitivity of AmeriFlux-based $\text{NMI}(\theta_s, \text{fPET})/\text{NMI}(\theta_v, \text{fPET})$**

250 As mentioned in Sect. 2.1, an important concern is the impact of interpolation errors used to estimate 0–40 cm θ_v from
 251 AmeriFlux θ_s observations acquired at non-uniform depths. To ensure that different methods for calculating
 252 AmeriFlux θ_v values do not affect the main conclusion of this study, we configured three cases for θ_v calculation, and
 253 compared their $\text{NMI}(\theta_s, \text{fPET})/\text{NMI}(\theta_v, \text{fPET})$ results in Fig. 2. Case I reflects the baseline use of the exponential
 254 filter described in Sect. 2.1. However, slight changes to AmeriFlux results are noted if alternative approaches are used.
 255 Specifically, AmeriFlux-based $\text{NMI}(\theta_v, \text{fPET})$ increases and closes the gap with $\text{NMI}(\theta_s, \text{fPET})$ if the bottom-layer
 256 soil moisture measurements are instead directly used as θ_v (Case II) or if 0–40 cm θ_v is based on the linear interpolation
 257 of the two AmeriFlux θ observations (Case III), the impact of this modest sensitivity on key results is discussed below.



258



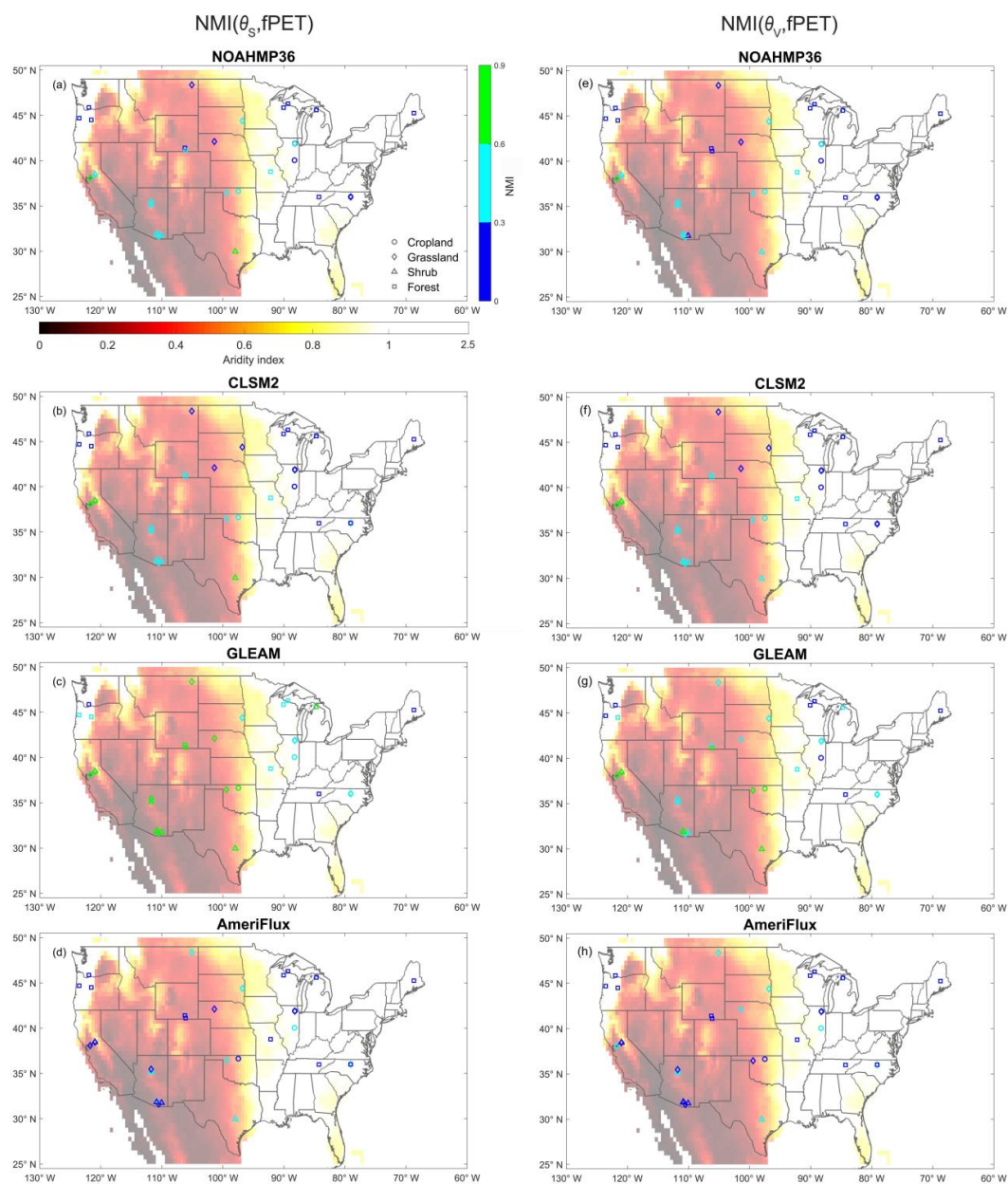
259 Fig.2 The θ /ET coupling strengths for summertime anomaly time series from AmeriFlux measurements using three different θ_v
260 calculation methods: (a) $\text{NMI}(\theta_s, \text{fPET})$ and $\text{NMI}(\theta_v, \text{fPET})$ individually and (b) $\text{NMI}(\theta_s, \text{fPET})$ divided by $\text{NMI}(\theta_v, \text{fPET})$ for
261 multiple θ_v cases. Case I is based on the application of an exponential filter to extrapolate 0–10 cm θ_s to a consistent 0–40 cm
262 bottom layer depth, while Cases II and III refer to the direct use of only the bottom layer measurement and a linear interpolation of
263 both the top and bottom layer, respectively, to calculate θ_v (see Sect. 2.1 for details on each case).

264 In addition, switching from GLEAM- to NARR-based PET when calculating fPET for AmeriFlux-based $\text{NMI}(\theta_s,$
265 $\text{fPET})$ and $\text{NMI}(\theta_v, \text{fPET})$ does not qualitatively change results and produces only a very slight (~6%) increase in the
266 median $\text{NMI}(\theta_s, \text{fPET})/\text{NMI}(\theta_v, \text{fPET})$ ratio.

267 3.3 Spatial distribution of $\text{NMI}(\theta_s, \text{fPET})$ and $\text{NMI}(\theta_v, \text{fPET})$

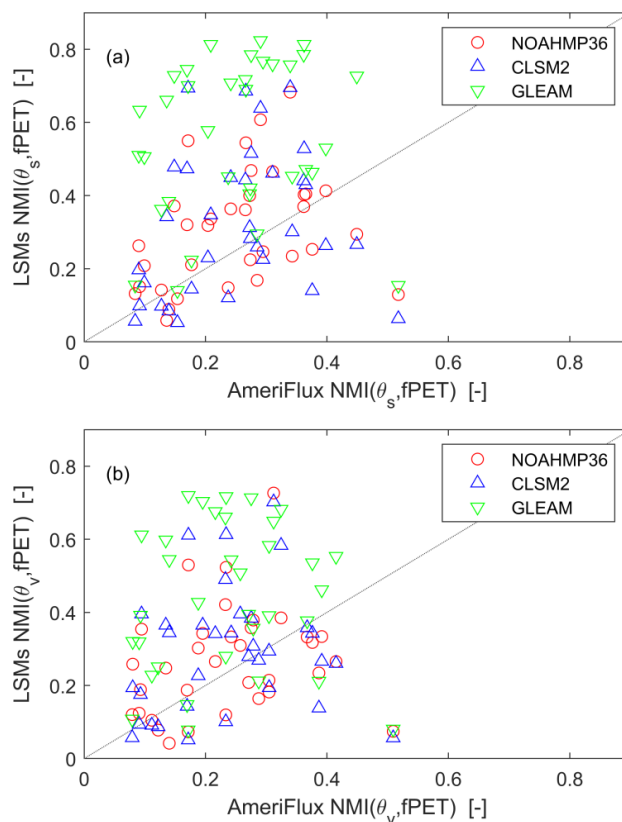
268 Figure 3 plots the spatial distribution of $\text{NMI}(\theta_s, \text{fPET})$ and $\text{NMI}(\theta_v, \text{fPET})$ results for each of the individual 34
269 AmeriFlux sites listed in Table 1. The climatic regime is represented by AI (aridity index) plotted as the background
270 color in Fig. 3. It can be seen in Fig. 3 that $\text{NMI}(\theta_s, \text{fPET})$ estimates from LSMs are spatially related to hydro-climatic
271 conditions, as NOAHMP and CLSM predict that θ_s is moderately coupled with fPET ($\text{NMI}(\theta_s, \text{fPET})$ of 0.3–0.5 [-])
272 in the arid Southwestern US ($\text{AI} < 0.2$) and only loosely coupled with fPET in the relatively humid Eastern US. A
273 similar decreasing trend of $\text{NMI}(\theta_s, \text{fPET})$ from the Southwestern to Eastern US is also captured by GLEAM.
274 However, as noted above, GLEAM generally overestimates $\text{NMI}(\theta_s, \text{fPET})$ and $\text{NMI}(\theta_v, \text{fPET})$ compared to
275 NOAHMP, CLSM and AmeriFlux. In contrast, a relatively weaker spatial pattern emerges in AmeriFlux-based
276 $\text{NMI}(\theta_s, \text{fPET})$ results. In addition, spatial patterns for $\text{NMI}(\theta_s, \text{fPET})$ are less defined than for $\text{NMI}(\theta_v, \text{fPET})$ in all
277 four datasets.

278 Scatterplots in Fig. 4 summarize the spatial relationship between LSM-based $\text{NMI}(\theta_s, \text{fPET})$ and $\text{NMI}(\theta_v, \text{fPET})$
279 results versus AmeriFlux observations. While observed levels of correlation in Fig. 4 are relatively modest, there
280 appears to be a significant level of spatial correspondence between modelled and observed NMI results – motivating
281 the need to better understand processes responsible for spatial variations in NMI results.



282

283 Fig. 3 NMI(θ_s , fPET) (left column) and NMI(θ_v , fPET) (right column) estimates at AmeriFlux sites for: (a) NOAHMP, (b) CLSM,
 284 (c) GLEAM and (d) AmeriFlux. Marker color reflects NMI magnitudes and symbol type reflects local land cover type at each site.
 285 Background color shading reflects aridity index (AI) values.



286

287 **Fig. 4** Scatterplot of LSM-based (a) $\text{NMI}(\theta_s, \text{fPET})$ and (b) $\text{NMI}(\theta_v, \text{fPET})$ results versus AmeriFlux observations.

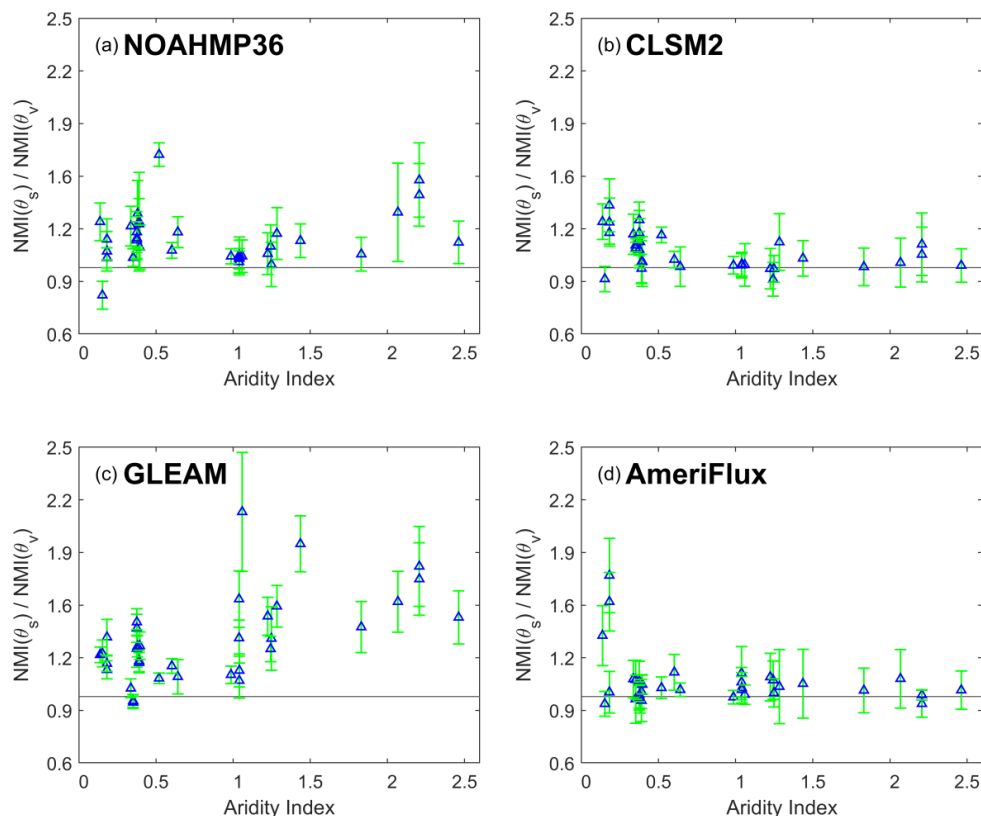
288 **3.4 Sensitivity of $\text{NMI}(\theta_s, \text{fPET})/\text{NMI}(\theta_v, \text{fPET})$ ratio to climatic conditions**

289 Figure 5 further summarizes the ratio of $\text{NMI}(\theta_s, \text{fPET})$ and $\text{NMI}(\theta_v, \text{fPET})$ as a function of AI for all four products
290 (NOAHMP, CLSM, GLEAM and AmeriFlux). Error bars represent the standard deviation of sampling errors
291 calculated from a 500-member bootstrapping analysis. **With increasing AI, there is a decreasing trend in surface and**
292 **vertically integrated θ/ET coupling within both NOAHMP and CLSM. This decreasing trend is particularly clear when**
293 **AI is below 1.0 [-]. NOAHMP, CLSM and GLEAM estimates of $\text{NMI}(\theta_s, \text{fPET})$ are generally higher than $\text{NMI}(\theta_v,$
294 **$\text{fPET})$ in all climatic conditions.** There is relatively lower sensitivity to aridity captured in the AmeriFlux
295 measurements, as the $\text{NMI}(\theta_s, \text{fPET})/\text{NMI}(\theta_v, \text{fPET})$ ratio still approximates one under semiarid conditions (i.e., AI
296 < 0.5 [-]).**

297 Connecting these findings to spatial distribution of $\text{NMI}(\theta_s, \text{fPET})$ and $\text{NMI}(\theta_v, \text{fPET})$ (Fig. 3), it is confirmed that
298 the relative magnitudes of $\text{NMI}(\theta_s, \text{fPET})$ and $\text{NMI}(\theta_v, \text{fPET})$ for all three LSMs are spatially related to hydro-climatic
299 regimes (although in fundamentally different ways). In contrast, this link is weaker in the AmeriFlux measurements
300 which, except for a small fraction of very low AI sites, do not appear to vary as a function of AI. These conclusions



301 are not qualitatively impacted by looking at $NMI(\theta_s, fPET)$ and $NMI(\theta_v, fPET)$ differences, as opposed to their ratio
302 as in Fig. 5, or by looking at $R(\theta_s, fPET)$ and $R(\theta_v, fPET)$ instead of NMI.



303

304 Fig. 5 For a) NOAHMP, (b) CLSM, (c) GLEAM and (d) AmeriFlux estimates, the ratio of $NMI(\theta_s, fPET)$ and $NMI(\theta_v, fPET)$ as
305 a function of AI across all AmeriFlux sites.

306 4 Discussion and conclusion

307 Since transpiration dominates the global ET (Jasechko et al., 2013), deep-layer soil moisture (θ_v) is generally
308 considered to contain more ET information than that of surface soil moisture (θ_s) – given plant transpiration is
309 balanced by root water uptake from deeper soils (Seneviratne et al., 2010). However, this assumption is rarely tested
310 using models and/or observations. Here, we apply normalized mutual information (NMI) to examine how the vertical
311 support of a soil moisture product impacts its relationship with concurrent surface ET.

312 Specifically, using AmeriFlux ground observations, we examine whether (NMI-based) estimates of LSM θ_s versus
313 ET and θ_v versus ET coupling strength accurately reflect observations acquired at a range of AmeriFlux sites. In
314 general, compared to the baseline case of exponential filter extrapolated 40-cm bottom layer θ_v , LSMs agree with
315 AmeriFlux observations in that the overall fPET information contained in θ_s is slightly higher than that of θ_v (Fig. 1).



316 However, the sensitivity analysis showed this difference between $\text{NMI}(\theta_s, \text{fPET})$ and $\text{NMI}(\theta_v, \text{fPET})$ diminishes when
317 using different methods for calculating θ_v using AmeriFlux observations (Fig. 2). As a result, this result should be
318 viewed with caution.

319 While NOAHMP and CLSM derived $\text{NMI}(\theta_s, \text{fPET})$ and $\text{NMI}(\theta_v, \text{fPET})$ results are generally consistent with the
320 AmeriFlux observations, GLEAM overestimates $\text{NMI}(\theta_s, \text{fPET})$, $\text{NMI}(\theta_v, \text{fPET})$, and the ratio $\text{NMI}(\theta_s,$
321 $\text{fPET})/\text{NMI}(\theta_v, \text{fPET})$ relative to observations. Although both LSMs and GLEAM are based on the same classical
322 two-section (soil moisture-limited and energy-limited) ET regimes framework (Sect. 2.2), they differ in two
323 fundamental aspects. First, the evaporative stress is represented as a more direct and strong function of soil moisture
324 in GLEAM - see Eqs. (4) and (5) - which leads to the overestimation of θ/ET coupling strength. This is consistent
325 with our results that GLEAM generally overestimates $\text{NMI}(\theta_s, \text{fPET})$ and $\text{NMI}(\theta_v, \text{fPET})$ consistently across all land
326 covers, compared to AmeriFlux-based estimates.

327 On the other hand, NOAHMP and CLSM approximate ET in the manner of biophysical models, and expresses
328 biophysical control on ET through the stomatal resistance r_s , which is a function of multiple limiting factors including
329 θ . Therefore, the more complex ET scheme employed by NOAHMP and CLSM would seem to mitigate the
330 overestimation of $\text{NMI}(\theta_s, \text{fPET})$ and $\text{NMI}(\theta_v, \text{fPET})$, as other relevant factors besides θ (such as temperature, foliage
331 nitrogen) are also considered in determining maximum carboxylation rate V_{\max} and stomatal resistance r_s - and
332 consequently more realistic actual ET. Secondly, the stress factor β in both LSMs considers the cumulative effects of
333 θ conditions along different layers (Eq. (1)), while the corresponding S factor in GLEAM only uses the wettest soil
334 layer condition, which is top layer at most sites. This likely explains the overestimation of the $\text{NMI}(\theta_s, \text{fPET})/\text{NMI}(\theta_v,$
335 $\text{fPET})$ ratio by GLEAM.

336 Although the median values of $\text{NMI}(\theta_s, \text{fPET})$ and $\text{NMI}(\theta_v, \text{fPET})$ predicted by NOAHMP and CLSM are general in
337 line with AmeriFlux observations, they are more spatially related to hydro-climatic conditions (as summarized by AI)
338 than their counter parts acquired from AmeriFlux measurements. Seen from the plot of $\text{NMI}(\theta_s, \text{fPET})/\text{NMI}(\theta_v, \text{fPET})$
339 ratio as a function of AI (Fig. 5), the modelled and observed $\text{NMI}(\theta_s, \text{fPET})/\text{NMI}(\theta_v, \text{fPET})$ ratio median decreases
340 with increasing AI, and the decreasing trend is particularly clear when AI is lower than 1.0 [-]. In contrast, there is
341 relatively lower sensitivity to aridity exhibited in the AmeriFlux measurements.

342 These results provide several key insights into future land-atmosphere coupling analysis and LSM development. First,
343 all the datasets – both model-based and ground-observed – indicates that θ_s contain at least as much ET information
344 as θ_v . Hence, remote-sensing land surface soil moisture datasets are suitable, and should be considered, for analyzing
345 the general interaction between land and atmosphere, e.g., soil moisture – air temperature coupling (Dong and Crow,
346 2019) and the interplay of soil moisture and precipitation (Yin et al., 2014). Additionally, future generations of
347 GLEAM may consider more sophisticated evaporation stress functions, which may improve its accuracy in
348 representing soil's control on local ET. This may, in turn, improve the accuracy of GLEAM ET product. Finally, our
349 results demonstrate that modeled θ/ET is highly sensitive to hydro-climates, compared to observed relationships.



350 Modifying the model structures to reduce such sensitivity might be necessary for accurately representing the
351 interaction of land surface and atmosphere across different climate zone. This may lead to more realistic projections
352 of future drought-induced heatwaves, when coupled with general circulation models.

353 **Data availability**

354 Ground-based soil moisture and surface flux data are available from <http://ameriflux.ornl.gov/>. GLEAM dataset is
355 available from <https://www.gleam.eu/>. LSMs simulations of NOAHMP and CLSM used in this study are available by
356 contacting the authors.

357 **Author contributions**

358 Jianxiu Qiu and Wade T. Crow conceptualized the study. Jianzhi Dong helped preparing the LSMs simulation. Grey S.
359 Nearing assisted in the mutual information analysis. Jianxiu Qiu carried out the analysis and wrote the first draft
360 manuscript, and Wade T. Crow refined the work. All authors contributed to the analysis, interpretation and writing.

361 **Competing interests**

362 The authors declare that they have no conflict of interest.

363 **Acknowledgments**

364 This work was supported by National Natural Science Foundation of China (Grant Nos. 41501450, 51779278) and
365 Natural Science Foundation of Guangdong Province, China (Grant No. 2016A030310154).

366 **References**

367 Albergel, C., Rüdiger, C., Pellarin, T., Fritz, N., and Froissard, F.: From near-surface to root-zone soil moisture using
368 an exponential filter: an assessment of the method based on in-situ observations and model simulations, *Hydrol. Earth
369 Syst. Sci.*, 12, 1323–1337, doi: 10.5194/hess-12-1323-2008, 2008.

370 Basara, J. B. and Crawford, K. C.: Linear relationships between root - zone soil moisture and atmospheric processes
371 in the planetary boundary layer, *J. Geophys. Res.*, 107, 4274, doi:10.1029/2001JD000633, 2002.

372 Boden, T. A., Krassovski, M., and Yang, B.: The AmeriFlux data activity and data system: an evolving collection of
373 data management techniques, tools, products and services, *Geosci. Instrum. Meth. Data Syst.*, 2, 165–176, doi:
374 10.5194/gi-2-165-2013, 2013.

375 Cover, T. M. and Thomas, J. A.: *Elements of information theory*, John Wiley & Sons, New York, 1991.



- 376 Crow, W.T., Lei, F., Hain, C., Anderson, M.C., Scott, R.L., Billesbach, D., and Arkebauer, T.: Robust estimates of
377 soil moisture and latent heat flux coupling strength obtained from triple collocation, *Geophys. Res. Lett.*, 42, 8415–
378 8423, doi: 10.1002/2015GL065929, 2015.
- 379 Dirmeyer, P. A., Chen, L., Wu, J., Shin, C. - S., Huang, B., and Cash, B. A.: Verification of land - atmosphere
380 coupling in forecast models, reanalyses, and land surface models using flux site observations, *J. Hydrometeorol.*,
381 19, 375–392, doi: 10.1175/JHM-D-17-0152.1, 2018.
- 382 Dong, J. and Crow, W.T.: Use of satellite soil moisture to diagnose climate model representations of European soil
383 moisture - air temperature coupling strength, *Geophys. Res. Lett.*, 45, 12884–12891, doi: 10.1029/2018GL080547,
384 2018.
- 385 Dong, J. and Crow, W.T.: L-band remote-sensing increases sampled levels of global soil moisture - air temperature
386 coupling strength, *Remote Sens. Environ.*, 22, 51–58, doi: 10.1016/j.rse.2018.10.024, 2019.
- 387 Dong, J., Crow, W.T., Reichle, R., Liu, Q., Lei, F., and Cosh, M.: A global assessment of added value in the SMAP
388 Level-4 soil moisture product relative to its baseline land surface model, in press, *Geophys. Res. Lett.*, 2019.
- 389 Entekhabi, D., Njoku, E.G., O'Neill, P.E., Kellogg, K.H., Crow, W.T., Edelstein, W.N., Entin, J.K., Goodman, S.D.,
390 Jackson, T.J., and Johnson, J.: The Soil Moisture Active Passive (SMAP) mission, *Proc. IEEE.*, 98, 704–716, doi:
391 10.1109/jproc.2010.2043918, 2010.
- 392 Ford, T. W., Wulff, C. O., and Quiring, S. M.: Assessment of observed and model - derived soil moisture -
393 evaporative fraction relationships over the United States Southern Great Plains, *J. Geophys. Res.*, 119, 6279–6291,
394 doi: 10.1002/2014JD021490, 2014a.
- 395 Ford, T. W. and Quiring, S. M.: In situ soil moisture coupled with extreme temperatures: A study based on the
396 Oklahoma Mesonet, *Geophys. Res. Lett.*, 41, 4727–4734, doi: 10.1002/2014gl060949, 2014b.
- 397 Hirschi M., Mueller, B., Dorigo, W., and Seneviratne, S. I.: Using remotely sensed soil moisture for land–atmosphere
398 coupling diagnostics: The role of surface vs. root-zone soil moisture variability, *Remote Sens. Environ.*, 154, 246–
399 252, doi: 10.1016/j.rse.2014.08.030, 2014.
- 400 Jasechko, S., Sharp, Z. D., and Gibson, J. J.: Terrestrial water fluxes dominated by transpiration, *Nature*, 2013, 496,
401 347–350, doi: 10.1038/nature11983, 2013.
- 402 Kerr, Y.H., Waldteufel, P., Wigneron, J.P., Martinuzzi, J., Font, J., and Berger, M.: Soil moisture retrieval from space:
403 the Soil Moisture and Ocean Salinity (SMOS) mission, *IEEE Trans. Geosci. Remote Sens.*, 39, 1729–1735, doi:
404 10.1109/36.942551, 2001.
- 405 Koster, R. D., Suarez, M. J., Ducharne, A., Stieglitz, M., and Kumar, P.: A catchment-based approach to modeling
406 land surface processes in a general circulation model: 1. Model structure, *J. Geophys. Res.*, 105, 24809–24822, doi:
407 10.1029/2000JD900327, 2000.



- 408 Koster, R. D., Schubert, S. D., and Suarez, M. J.: Analyzing the concurrence of meteorological droughts and warm
409 periods, with implications for the determination of evaporative regime, *J. Climate.*, 22, 3331–3341,
410 doi:10.1175/2008JCLI2718.1, 2009.
- 411 Kullback, S. and Leibler, R. A.: On information and sufficiency, *Ann. of Math. Stat.*, 22, 79–86, doi:
412 10.1214/aoms/1177729694, 1951.
- 413 Kumar, S. V., Peters-Lidard, C. D., Tian, Y., Houser, P. R., Geiger, J., Olden, S., Lighty, L., Eastman, J. L., Doty, B.,
414 Dirmeyer, P., dams, J.A., Mitchell, K., Wood, E. F., and Sheffield, J.: Land information system: An interoperable
415 framework for high resolution land surface modeling, *Environ. Modell. Softw.*, 21, 1402–1415, doi:
416 10.1016/j.envsoft.2005.07.004, 2006.
- 417 Lei, F., Crow, W.T., Holmes, T., Hain, C., and Anderson, M.: Global investigation of soil moisture and latent heat
418 flux coupling strength, *Water Resources Research.*, 54, 8196–8215, doi:10.1029/2018WR023469, 2018.
- 419 Mahrt, L. and Ek, M.: The influence of atmospheric stability on potential evaporation, *J. Clim. Appl.*
420 *Meteorol.*, 23, 222–234, doi:10.1175/1520 - 0450(1984)023<0222:TIOASO>2.0.CO;2, 1984.
- 421 Martens, B., Miralles, D. G., Hans, L., Robin, V. D. S., and de Jeu, J. R. A. M.: Gleam v3: satellite-based land
422 evaporation and root-zone soil moisture, *Geosci. Model Dev.*, 10, 1903–1925, doi: 10.5194/gmd-10-1903-2017, 2017.
- 423 Miralles, D. G., Holmes, T. R. H., De Jeu, R. A. M., Gash, J. H., Meesters, A. G. C. A., and Dolman, A. J.: Global
424 land-surface evaporation estimated from satellite-based observations, *Hydrol. Earth Syst. Sci.*, 15, 453–469,
425 doi:10.5194/hess-15-453-2011, 2011.
- 426 Nearing, G. S., Yatheendradas, S., and Crow, W. T.: Nonparametric triple collocation, *Water Resour. Res.*, 53, 5516–
427 5530, doi: 10.1002/2017WR020359, 2017.
- 428 Nearing, G. S., Ruddell, B. L., Clark, M. P., Nijssen, B., and Peters-Lidard, C. D.: Benchmarking and Process
429 Diagnostics of Land Models, *J. Hydrometeorol.*, 19, 1835–1852, doi: 10.1175/JHM-D-17-0209.1, 2018.
- 430 Nearing, G. S., Mocko, D. M., Peters-Lidard, C. D., Kumar, S. V., and Xia, Y.: Benchmarking NLDAS-2 Soil
431 Moisture and Evapotranspiration to Separate Uncertainty Contributions, *J. Hydrometeorol.*, 17, 745–759, doi:
432 10.1175/JHM-D-15-0063.1, 2016.
- 433 Nearing, G. S. and Gupta, H. V.: The quantity and quality of information in hydrologic models, *Water Resour. Res.*,
434 51, 524–538, doi: 10.1002/2014WR015895, 2015.
- 435 Nearing, G. S., Gupta, H. V. Crow, W. T., and Gong, W.: An approach to quantifying the efficiency of a Bayesian
436 filter, *Water Resour. Res.*, 49, 2164–2173, doi: 10.1002/wrcr.20177. 2013.
- 437 Niu, G. Y., Yang, Z. L., Mitchell, K. E., Chen, F., Ek, M. B., Barlage, M., Kumar, A., Manning, K., Niyogi, D., Rosero,
438 E., Tewari, M., and Xia, Y. L.: The community Noah land surface model with multiparameterization options (Noah-
439 MP): 1. Model description and evaluation with local-scale measurements, *J. Geophys. Res.*, 116, 1248–1256,
440 doi:10.1029/2010jd015139, 2011.



- 441 Paninski, L.: Neural Computation, Estimation of Entropy and Mutual Information., 15, 1191–1253, doi:
442 10.1162/089976603321780272, 2003.
- 443 Priestley, J. H. C. and Taylor, J.: On the assessment of surface heat flux and evaporation using large-scale parameters,
444 Mon.Weather Rev., 100, 81–92, doi: 10.1175/1520-0493(1972)1002.3.CO;2, 1972.
- 445 Qiu, J., Crow, W. T., and Nearing, G. S.: The impact of vertical measurement depth on the information content of soil
446 moisture for latent heat flux estimation, J. Hydrometeorol., 17, 2419–2430, doi: 10.1175/JHM-D-16-0044.1, 2016.
- 447 Qiu, J., Crow, W. T., Nearing, G. S., Mo, X., and Liu, S.: The impact of vertical measurement depth on the information
448 content of soil moisture time series data, Geophys. Res. Lett., 41, 4997–5004, doi: 10.1002/2014GL06001, 2014.
- 449 Scott, D. W.: Multivariate density estimation and visualization, in Handbook of Computational Statistics: Concepts
450 and Methods, Springer, New York, 2014.
- 451 Seneviratne, S. I., Wilhelm, M., Stanelle, T., Hurk, B., Hagemann, S., and Berg, A.: Impact of soil moisture - climate
452 feedbacks on CMIP5 projections: First results from the GLACE - CMIP5 experiment, Geophys. Res. Lett., 40, 5212–
453 5217, doi: 10.1002/grl.50956, 2013.
- 454 Seneviratne, S. I., Corti, T., Davin, E. L., Hirschi, M., Jaeger, E. B., and Lehner, I.: Investigating soil moisture–climate
455 interactions in a changing climate: A review, Earth-Sci. Rev., 99, 125–161, doi:10.1016/j.earscirev.2010.02.004, 2010.
- 456 Shannon, C. E.: A mathematical theory of communication, Bell Labs Tech. J., 27, 379–423, doi: 10.1002/j.1538–
457 7305.1948.tb00917.x, 1948.
- 458 Wagner, W., Lemoine, G., and Rott, H.: A method for estimating soil moisture from ERS scatterometer and soil data,
459 Remote Sens. Environ., 70, 191–207, doi: 10.1016/S0034-4257(99)00036-X, 1999.
- 460 Yin, J., Porporato, A., and Albertson, J., Interplay of climate seasonality and soil moisture-rainfall feedback, Water
461 Resour. Res., 50, 6053–6066, doi: 10.1002/2013WR014772, 2014.